J. Fluid Mech. (2007), *vol.* 571, *pp.* 33–57.
doi:10.1017/S0022112006003004 Printed in the United Kingdom

Competitive displacement of thin liquid films on chemically patterned substrates

By RICHARD D. LENZ AND SATISH KUMAR

Department of Chemical Engineering and Materials Science, University of Minnesota, 151 Amundson Hall, 421 Washington Avenue SE, Minneapolis, MN 55455, USA

(Received 30 December 2005 and in revised form 16 June 2006)

The behaviour of the interface between stratified thin liquid films bounded by parallel solid surfaces and subject to van der Waals forces which drive dewetting is studied in this work. Chemically homogeneous surfaces are considered first; this is followed by an investigation of chemically heterogeneous surfaces. The lubrication approximation is applied to obtain a single nonlinear evolution equation which describes the interfacial behaviour, and both the linear stability and nonlinear development of the interface are examined. The sensitivity of the interfacial rupture time to problem parameters such as the viscosity ratio, initial interfacial height, interfacial tension, and magnitude of the van der Waals forces is characterized in detail for the homogeneous case. This serves as a basis for a study of the heterogeneous case, where the strong dependence of the rupture time on the length scale of the heterogeneity is found to be relatively independent of changes in the remaining problem parameters. The mechanisms underlying the rupture-time behaviour are also explored in detail. The results suggest a route by which one liquid can become emulsified in the other, and may be beneficial to industrial processes such as lithographic printing which are based on wettability phenomena.

1. Introduction

The study of thin liquid films has been motivated by their ubiquity. These films occur both naturally and industrially, where the interest may be in maintaining a stable film in a coating process or in controlling dewetting behaviour in order to create novel nanostructures or microstructures (Kargupta & Sharma 2002). An important extension of thin-liquid-film studies is the case where the film is not bounded by air at its free surface but by another thin liquid film adjacent to a solid surface. Such stratified thin liquid films between parallel surfaces may be subject to a competitive displacement, which occurs when both films are subject to van der Waals forces that would tend to rupture a solitary film. The rupture of one film occurs via displacement by the other film, and a competition exists between the two films to determine which displaces the other. An additional competition becomes important when one of the surfaces is chemically patterned. In this case, the length scales of the more-wettable and less-wettable areas of the surface will compete with the system's natural horizontal length scale, given by the wavelength of the disturbance mode that grows most rapidly on an unpatterned surface, to determine the mechanism by which rupture occurs. A study of these competitions is the subject of this work.

The lithographic printing process is a practical motivation for examining the system described above. As the world's leading technique for the creation of printed mass

media, lithographic printing is being explored for the mass-production of electronic materials (Harrey *et al.* 1999; Leyland, Evans & Harrison 2002), but its fundamentals remain poorly understood. Successful operation of the process (MacPhee 1998) relies on the transfer of ink from a carrier roll to the hydrophobic areas of a chemically patterned printing plate through a thin barrier film of a water-like fountain solution. Defect-free printing requires that the fountain-solution film maintains stability on the hydrophilic 'non-image' regions, but becomes unstable and ruptures on the hydrophobic 'image' regions. The fountain solution preferentially wets the hydrophilic areas, whereas the ink preferentially wets the hydrophobic areas. The models presented in this paper provide a starting point for the understanding of this mechanism, in which ink displaces the fountain-solution layer to form an emulsion on the image areas of the printing plate.

Before proceeding, a review of prior work is necessary to put our own work into the proper context. Early theoretical analyses of thin liquid films were conducted by Vrij (1966) and Sheludko (1967), who explored the physical mechanisms that lead to the rupture of free films and of films on chemically homogeneous substrates. They laid the groundwork for subsequent studies, many of which were based on simplifying the governing equations via the lubrication approximation (Benney 1966; Oron, Davis & Bankoff 1997). This method was employed by Ruckenstein & Jain (1974) to examine the linear stability of a substrate-bound film subject to van der Waals forces that drive dewetting and by Williams & Davis (1982) to perform a full nonlinear simulation of a similar film approaching rupture. The van der Waals forces are included in these models as a body-force term that is derived by taking the gradient of a disjoining pressure. The nonlinear evolution equation derived by Williams & Davis (1982) was shown by Zhang & Lister (1999) to exhibit an infinite number of similarity solutions near film rupture, and the linear stability of such solutions was studied by Witelski & Bernoff (1999). Sharma & Jameel (1993) examined the case in which a film was subjected to polar forces in addition to these apolar van der Waals forces. Polar forces are of shorter range, and their inclusion in the model leads to scenarios in which a film can reach a phase-separated equilibrium rather than rupture. The behaviour of films in the presence of insoluble (Jensen & Grotberg 1992) and soluble (Jensen & Grotberg 1993) surfactants has been considered, for cases where the flows are generated by surface-tension gradients due to heterogeneous surfactant concentration. Evolution equations have also been derived for free films in the presence of insoluble (de Wit, Gallez & Christov 1994) and soluble (Matar 2002) surfactants, and more recently, for films on flexible walls (Matar & Kumar 2004) and elastomers (Matar, Gkanis & Kumar 2005).

The behaviour of stratified thin liquid films on chemically homogeneous surfaces is a direct extension of the above body of work. An early extension was provided by Yiantsios & Higgins (1991), who derived a two-layer evolution equation for a single liquid film bounded above by a semi-infinite viscous liquid. Actual stratified films with two free surfaces have been examined in the context of tear films found in the human eye. Sharma & Ruckenstein (1985) proposed a mechanism for rupture in such a bilayer based on a two-step process, the key feature being the rupture of the lower mucus layer due to van der Waals forces, followed by rapid rupture of the aqueous top layer on the hydrophobic cornea substrate. This idea was later developed more fully by the same authors using analytical methods (Sharma & Ruckenstein 1986*a*, *b*). A full nonlinear simulation of the problem was performed by Zhang, Matar & Craster (2003), who considered the lower mucus layer to be shear-thinning. Independently of the literature on tear films, the stability of general stratified liquid layers with two free surfaces has been examined (Danov *et al.* 1998*a*, *b*; Paunov *et al.* 1998),

as have the different pathways to rupture, which depend on which layer ruptures more rapidly (Pototsky *et al.* 2004). Fisher & Golovin (2005) recently performed a nonlinear stability analysis and found that these layers may evolve to form a series of drops separated by thin wetting layers even in the absence of short-range repulsion. Only a single free surface is encountered in the work of Joo & Hsieh (2000), who considered the case of two liquids held between parallel solid surfaces and subject to both a temperature gradient and van der Waals forces. More recently Merkt *et al.* (2005) examined a similar problem, focusing on the effects of gravity, electrostatic fields, and thermocapillarity on interfacial stability. They did not include the van der Waals forces which drive rupture, instead using them to stabilize the films in order to examine pattern formation at long times.

Sharma and coworkers have applied the lubrication approximation to examine rupture and pattern formation in solitary thin liquid films on chemically heterogeneous substrates (Konnur, Kargupta & Sharma 2000; Kargupta, Konnur & Sharma 2000; Zope, Kargupta & Sharma 2001). They found that a film lying on a substrate with alternating more-wettable and less-wettable stripes would actually rupture more rapidly than a film lying on a chemically homogeneous surface of the less-wettable material. In their analysis, the rupture time of a film was determined as being independent of the length scale of a less-wettable patch on the substrate, as long as the length scale was greater than a critical value.

A discussion of the experimental work on thin-liquid-film rupture was given by Seemann, Herminghaus & Jacobs (2001). They noted the difficulty in separating 'spinodal' dewetting, predicted by theoretical work like that described above, from dewetting by external nucleation. Kheshgi & Scriven (1991) visualized dewetting nucleated externally by dust particles and discussed the mechanisms by which this occurs. True spinodal dewetting modes were observed by Bischof *et al.* (1996) in thin gold films. They detected undulations with the same length scale as predicted by theory. Stange, Evans & Hendrickson (1997) used atomic-force microscopy to verify the expected exponential growth rate associated with spinodal dewetting in thin polymer films. They also compared the relative importance of the two rupture mechanisms in a clean-room environment. More recently, Karapanagiotis & Gerberich (2005) used a similar technique to provide a detailed account of the three-dimensional morphology of spinodal dewetting.

The work described in this paper concerns stratified thin liquid films between chemically heterogeneous solid surfaces. We first extend the work of Joo & Hsieh (2000) by performing a more comprehensive study of the stratified system with chemically homogeneous surfaces (in the absence of thermocapillary effects). The subsequent introduction of chemical heterogeneity bridges a gap between the work of Joo & Hsieh (2000) and the work of Sharma and co-workers (Konnur *et al.* 2000; Kargupta *et al.* 2000; Zope *et al.* 2001). We focus on the case in which the lower surface is periodically patterned with regions that the bottom liquid will find less-wettable and more-wettable. We shall find that the rupture times for this lower liquid have a clear dependence on the length scales of both the less- and more-wettable regions relative to the wavelength of the most rapidly growing disturbance for a homogeneous surface. The physical mechanisms that lead to this dependence are elucidated quantitatively by examining the different contributions to the liquid flow rates during interfacial evolution. We also find that the dependence is remarkably robust to variations in the remaining parameters. The problem is formulated in § 2, results are presented and discussed for the homogeneous and heterogeneous cases in § 3 and § 4, respectively, and conclusions are given in § 5.

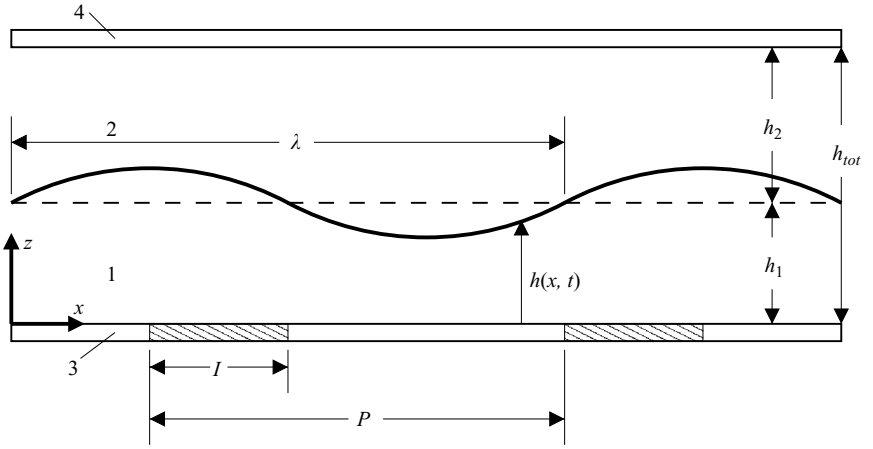

FIGURE 1. Schematic representation of the problem setup, with all labelled quantities in dimensional form.

2. Problem formulation

We consider two stratified Newtonian liquids between two stationary parallel solid surfaces; the lower liquid is labelled 1 and the upper liquid is labelled 2 (figure 1). Making an analogy with lithographic printing, the liquids would represent the fountain solution and the ink, respectively. The lower solid surface, labelled as 3, is chemically patterned in a periodic way for studies with heterogeneous surfaces. For this case, intervals of dimensional length I are patterned in such a way that liquid 2 will wet them whereas liquid 1 will not. Each interval represents an 'image' region of a lithographic printing plate, while the remaining surface of solid 3 is neutral to both liquids, representing 'non-image' areas. The terms 'image' and 'non-image' will be used throughout this paper to describe regions to which liquid 1 is less-wettable and more-wettable, respectively. The left-hand edges of each consecutive image region are separated by the period size P. The surface of solid 4, as with the non-image areas of surface 3, is considered neutral to both liquids when we examine heterogeneous surfaces. The homogeneous-surface limit occurs when either $I = 0$ or $I = P$.

2.1. *Governing equations*

The gap between the two solid surfaces, h_{tot}, is taken to be much smaller than the wavelength of a typical disturbance, λ, so that the lubrication approximation may be applied. Thus we define the small parameter $\epsilon = h_{tot}/\lambda \ll 1$. This leads to the following scaling for our dimensionless lengths x, z and velocities u_i, w_i:

$$x = \frac{\epsilon \tilde{x}}{h_{tot}}, \qquad z = \frac{\tilde{z}}{h_{tot}}, \qquad u_i = \frac{\tilde{u}_i \rho_1 h_{tot}}{\mu_1}, \qquad w_i = \frac{\tilde{w}_i \rho_1 h_{tot}}{\epsilon \mu_1}, \tag{2.1}$$

where the subscript i indicates to which liquid the quantity corresponds, μ denotes viscosity, ρ denotes density and the tilde is used to indicate a dimensional variable. The scales for the dimensionless time and stress variables are

$$t = \frac{\epsilon \tilde{t} \mu_1}{h_{tot}^2 \rho_1}, \qquad (p_i, \phi_i) = (\tilde{p}_i, \tilde{\phi}_i) \frac{\epsilon h_{tot}^2 \rho_1}{\mu_1^2}. \tag{2.2}$$

Here ϕ is the van der Waals component of the disjoining pressure; it is a potential

energy per unit volume which takes a form first obtained by Hamaker (1937) and later applied by Vrij (1966) and Sheludko (1967). For a single particle of material 1 suspended a distance h above a semi-infinite solid of material 3, the expression for the disjoining pressure is $\phi = A_{13}/h^3$, where A_{13} is the dimensionless Hamaker constant representing the magnitude of the van der Waals attraction between particle 1 and solid 3. The scaling for the Hamaker constants is $\epsilon \tilde{A}_{ij}\rho_1/\mu_1^2 h_{tot}$, where $\tilde{A}_{ij}$ is a dimensional Hamaker constant representing the attraction between materials i and j. In our analysis, it is important to use expressions for the van der Waals attraction felt by single parcels of each liquid at the 1–2 interface, subject to their interactions with all four materials present in the problem. These are (Kumar & Matar 2004):

$$\phi_1 = \phi_{11}^{\infty} + \phi_{12}^{\infty} + \frac{A_{11} - A_{13}}{h^3} + \frac{A_{12} - A_{14}}{(1-h)^3}, \tag{2.3}$$

$$\phi_2 = \phi_{22}^{\infty} + \phi_{12}^{\infty} + \frac{A_{12} - A_{23}}{h^3} + \frac{A_{22} - A_{24}}{(1-h)^3}, \tag{2.4}$$

where $h = h(x,t)$ is the interface height. Here ϕ_{ij}^{∞} is a constant representing the potential energy per unit volume felt by a particle of material i at the surface of a semi-infinite body of material j; it disappears when the gradients of the expressions are calculated.

The dimensional momentum balance for liquid i is given by

$$\rho_i(\partial_{\tilde{t}}\tilde{\boldsymbol{u}}_i + \tilde{\boldsymbol{u}}_i \cdot \nabla\tilde{\boldsymbol{u}}_i) = -\nabla(\tilde{p}_i + \tilde{\phi}_i) + \mu_i \nabla^2 \tilde{\boldsymbol{u}}_i, \tag{2.5}$$

where $\tilde{\boldsymbol{u}}_i$ is the velocity vector. We have omitted the gravitational body force, as the small gap distance renders it negligible with respect to capillary and van der Waals forces. We obtain the lubrication form of the momentum balance by substituting our dimensionless variables and dropping terms of order ϵ and smaller:

$$0 = -\partial_x \bar{p}_i + \frac{\mu_i}{\mu_1}\partial_z^2 u_i, \tag{2.6}$$

$$0 = \partial_z \bar{p}_i. \tag{2.7}$$

Here we have employed a reduced pressure, $\bar{p}_i$:

$$\bar{p}_i = p_i + \phi_i. \tag{2.8}$$

The stress balance at the liquid–liquid interface is given by

$$\boldsymbol{T}_1 \cdot \boldsymbol{n} - \boldsymbol{T}_2 \cdot \boldsymbol{n} = -\kappa\tilde{\gamma}\boldsymbol{n}, \tag{2.9}$$

where $\boldsymbol{T}_i$ is the stress tensor in liquid i, $\boldsymbol{n}$ is the vector normal to the interface directed into liquid 2, and κ is the interfacial curvature. The dimensionless normal and shear stress components in lubrication form are

$$3\gamma\partial_x^2 h = \bar{p}_2 - \bar{p}_1 - \phi_2 + \phi_1, \tag{2.10}$$

$$\mu_r \partial_z u_2 = \partial_z u_1, \tag{2.11}$$

γ being the dimensionless interfacial tension,

$$\gamma = \epsilon^3 \tilde{\gamma}\rho_1 h_{tot}/3\mu_1^2, \tag{2.12}$$

and μ_r the viscosity ratio μ_2/μ_1. Note that in order to keep a balance between

capillary forces and van der Waals forces, the factor ϵ^3 has been included in the scaling. Reduced pressures have also been incorporated into (2.10), so the expressions for the disjoining pressure now only appear in this normal-stress interfacial condition. No-slip and no-penetration conditions are applied at the solid surfaces. Equations (2.6), (2.7), (2.10), and (2.11) can be solved to obtain $u_1(z)$. The model is completed by using the kinematic boundary condition at $z = h(x, t)$,

$$w = \partial_t h + u\partial_x h, \tag{2.13}$$

which can be combined with the continuity equation $\partial_x u_i + \partial_z w_i = 0$ to yield a relationship between interfacial position and the flow rate of liquid 1:

$$0 = \partial_t h + \partial_x \int_0^h u_1 \, \mathrm{d}z. \tag{2.14}$$

Substitution of u_1 into (2.14) yields an evolution equation for $h(x, t)$:

$$0 = \partial_t h + \partial_x \left\{ \frac{[1 + (\mu_r - 1)h](1 - h)^3 h^3}{3 f(h, \mu_r)} \left[\partial_x(\phi_2 - \phi_1) + 3\gamma \partial_x^3 h \right] \right\}, \tag{2.15}$$

$f(h, \mu_r)$ being given by

$$f(h, \mu_r) = h^4 \mu_r^2 - (2h^4 - 4h^3 + 6h^2 - 4h)\mu_r + (h - 1)^4. \tag{2.16}$$

The two terms on the right-hand side of (2.15) are the temporal derivative of the interfacial height and the spatial derivative of the flow rate of liquid 1. The terms describing the relative magnitudes of the flow rate components are between the right-hand pair of square brackets. The first term drives flow through a gradient in the disjoining pressure. If we substitute (2.3) and (2.4) into this expression, we have

$$\partial_x(\phi_2 - \phi_1) = 3\partial_x h \left[\frac{A_2}{(1 - h)^4} + \frac{A_1}{h^4} \right] + \frac{\partial_x A_2}{(1 - h)^3} - \frac{\partial_x A_1}{h^3}, \tag{2.17}$$

where A_1 and A_2 are Hamaker constants that describe the magnitude of the van der Waals attraction of the liquid–liquid interface to surface 3 or surface 4, respectively. They are composed of the binary Hamaker constants used in (2.3) and (2.4):

$$A_1 = (A_{11} - A_{13}) + (A_{23} - A_{12}), \tag{2.18}$$

$$A_2 = (A_{22} - A_{24}) + (A_{14} - A_{12}). \tag{2.19}$$

Each set of terms within parentheses represents a competition between attractions that will determine the stability of the interface. For example, if A_{11} is greater than A_{13} then liquid 1 prefers contact with itself over contact with the lower bounding solid. This scenario would tend to destabilize the interface, as would a positive result from any of the other three competitions.

Our full evolution equation is given by (2.15), (2.16), and (2.17) and reduces in certain limits to evolution equations derived in prior works. For constant values of A_1 and A_2 in (2.17), it becomes

$$0 = \partial_t h + \partial_x \left\{ \frac{1 + (\mu_r - 1)h}{f(h, \mu_r)} \left[\partial_x h \left(A_2 \frac{h^3}{1 - h} + A_1 \frac{(1 - h)^3}{h} \right) + \gamma (1 - h)^3 h^3 \partial_x^3 h \right] \right\}, \tag{2.20}$$

which represents the homogeneous-surface limit analyzed by Joo & Hsieh (2000) and Merkt *et al.* (2005). It reduces to the equation for a single liquid film on a solid

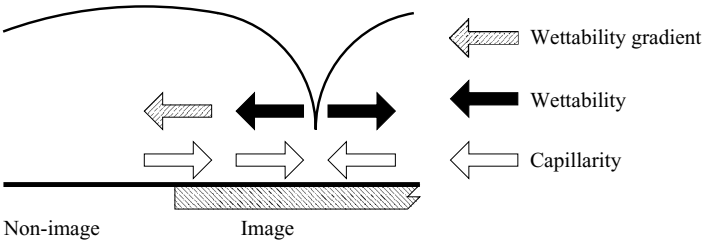

FIGURE 2. Schematic representation of the direction of flow in the lower liquid due to the three driving forces, the wettability gradient, the wettability, and capillarity. Capillarity acts to oppose both the other driving forces in an attempt to maintain a stable interface. The curve shows the interfacial height.

substrate on setting $A_2 = 0$ (no attraction to an upper bounding surface) and $\mu_r = 0$ (absence of a viscous top liquid):

$$0 = \partial_t h + A_1 \partial_x \left(\frac{\partial_x h}{h} \right) + \gamma \partial_x \left(h^3 \partial_x^3 h \right) \tag{2.21}$$

This equation was derived by Williams & Davis (1982) and later considered extensively by Burelbach, Bankoff & Davis (1988). In order to analyse concisely the effect of chemical patterning on interfacial rupture, we will consider another important limit of (2.15), in which we let $A_2 = 0$ and make $A_1 = A_1(x)$ ($\geqslant 0$). Therefore the liquid–liquid interface feels an attraction only to certain regions of surface 3, and the evolution equation becomes

$$0 = \partial_t h + \partial_x \left\{ \frac{(1 + (\mu_r - 1)h)(1-h)^3 h^3}{3 f(h, \mu_r)} \left[3 \partial_x h \left(\frac{A_1}{h^4} \right) - \frac{\partial_x A_1}{h^3} + 3 \gamma \partial_x^3 h \right] \right\}. \tag{2.22}$$

This problem is consistent with that encountered in lithographic printing.

The three terms within the square brackets in (2.22) give the relative strengths of the three different contributions to the flow rate of liquid 1. In order, they are the flow contributions due to wettability, wettability gradients, and capillarity. These contributions, illustrated schematically in figure 2, can be arrived at by an interrogation of each term. The wettability contribution, $3 \partial_x h \left(A_1 / h^4 \right)$, will be positive only when the interfacial slope is positive, and will have the largest magnitude when the slope is steep and the interfacial height is small. Thus it will have the largest magnitude near rupture, driving the flow to the right from locations right of the rupture ($\partial_x h > 0$), and to the left from locations left of the rupture ($\partial_x h < 0$). This flow-rate contribution will always act to facilitate rupture, therefore. Another contribution conducive to rupture comes from the wettability gradient, expressed as $-\partial_x A_1 / h^3$. This drives the flow of liquid 1 in the opposite direction to $\partial_x A_1$, or away from regions that the liquid–liquid interface finds attractive. It will be seen later that the magnitude of this term does not change substantially during the rupture process and plays an important role in initiating it. The capillarity contribution, $3 \gamma \partial_x^3 h$, opposes the rupture process through capillary pressure gradients. The third derivative of the interfacial height indicates that the gradient drives flow from regions of low or negative curvature (concave down) to regions of high or positive curvature (concave up). The flow is therefore driven towards the location of the eventual rupture, with its very positive curvature. The interfacial shape also varies subtly in the vicinity of the wettability gradients, resulting in a flow which opposes that caused by the wettability gradients. This is discussed quantitatively in § 4.2.

2.2. *Validity of the lubrication approximation*

If the wettability gradients are too sharp, the lubrication approximation can be expected to break down. The width of the transition region between image and non-image areas in our problem is given by a parameter δ, which is formally defined in the two different analytical expressions for $A_1(x)$ given in the following section, (2.23) and (2.24). A small value of δ indicates a large wettability gradient and the potential for breakdown of the theory. Most of the simulation results presented in this work use the value $\delta = 0.01$, whose meaning can be elucidated by considering a representative system. If liquids 1 and 2 are 100 nm thick with an interfacial tension of $24\,\mathrm{mN\,m^{-1}}$, solid 4 is neutral, and solid 3 is homogeneous with a typical Hamaker constant of $1 \times 10^{-20}\,\mathrm{J}$, then the wavelength of the fastest growing disturbance (derived using the linear theory to be described in § 3.1) is approximately 80 μm. Although this length is derived for the homogeneous case, we will later show that it still has a great deal of significance in the heterogeneous case. The above calculation results in $\epsilon = h_{tot}/\lambda = 2.5 \times 10^{-3}$ and a dimensional transition width $\tilde{\delta} = \delta h_{tot}/\epsilon = 4h_{tot}$. The length scale of the transition width is therefore still larger than the gap between the solid surfaces. In addition, the length scales of the image and non-image areas examined in our study are of the order of the characteristic horizontal length scale; this is some orders of magnitude greater than the transition width ($\lambda/\tilde{\delta} = 100$). Thus, even if lubrication theory is not formally valid in the proximity of the wettability gradients, it would still be expected to hold up across the majority of the problem domain.

Similar issues arise in the case where a surface has sharp topographical variations. Stillwagon & Larson (1988, 1990) examined the levelling of oil films over trenches on a stationary substrate and during a spin-coating process, obtaining good agreement between the experimental results and simulations based on a lubrication model. Pritchard, Scott & Tavener (1992) considered the flow of a viscous liquid down an inclined plane perturbed by consecutive surface humps and found substantial agreement between lubrication models and both experiments and full simulations. Similar experiments by Decré & Baret (2003) also yielded results in good agreement with lubrication models. Kalliadasis, Bielarz & Homsy (2000) acknowledged the potential shortcomings of applying lubrication theory when encountering steep topography but noted qualitative agreement with experiments in their parametric study. Solution of the Stokes equations by Mazouchi & Homsy (2001) confirmed that lubrication models become more quantitatively accurate with decreases in the capillary number.

2.3. *Numerical methods*

Simulations were performed using (2.20) for homogeneous surfaces and (2.22) for heterogeneous surfaces. In both cases, fourth-order centred finite differences with periodic boundary conditions were used to discretize the equations. Gear's algorithm was employed for time stepping, owing to its effectiveness in dealing with the inherent stiffness of the problem (Sharma & Jameel 1993; Konnur *et al.* 2000; Kargupta *et al.* 2000; Zope *et al.* 2001). The method automatically adjusts the time step, and this allows for large steps initially when the van der Waals driving force is weak but very small steps when the final rapid rupture occurs. In the homogeneous case, simulations were run with as few as 100 grid points per the most dangerous (i.e. fastest growing) wavelength, which was more than sufficient to maintain mass conservation. The heterogeneous case required more points to resolve the variations in $A_1(x)$, and convergence analyses indicated that rupture times did not change significantly when

the average height of the interface varied by less than 0.02 % at all times during the course of a simulation. This criterion was used to determine the number of grid points for each run, resulting in approximately 400 grid points per the most dangerous wavelength (on the basis of the value for the corresponding homogeneous case). An increase in the number of grid points from 400 to 500 results in a rupture time variation of less than 0.1 %, the criterion for rupture being a minimum film height of less than 1×10^{-4}.

The initial conditions for each type of surface differed. A single wave of dimensionless amplitude 0.05 was used as the initial interfacial position for the homogeneous case. The wavelength was set to be that predicted to grow most rapidly from linear theory (see § 3.1 below). This initial condition specifies the location where rupture will occur: always at the minimum in the initial interfacial height. This is acceptable for a simulation with homogeneous surfaces, where the time of rupture is the sole quantity of interest. For the heterogeneous case, the location of rupture is as important as the rupture time, so for this case a random initial condition was employed by averaging a series of Fourier modes with random phases and amplitudes. The largest wave was set to the length of the simulation domain, the remaining waves descending in wavelength until the smallest wave was just smaller than $\lambda_c/100$, where λ_c is the cutoff wavelength from linear theory. Multiple runs with different seed numbers for the random-number generator confirmed that the key features of the results are independent of the initial condition.

The domain of each simulation for the heterogeneous case consisted of a single centred image region of length I with a non-zero $A_1(x)$ value, bounded by non-image regions having $A_1(x) = 0$. Motivated by prior work on flows over surfaces with topographical variations (Stillwagon & Larson 1988), we employed an arctangent function to describe $A_1(x)$:

$$A_1(x) = \frac{A_1^{Im}}{\pi}\left[\arctan\left(\frac{x + I/2}{\delta}\right) - \arctan\left(\frac{x - I/2}{\delta}\right)\right]. \tag{2.23}$$

This expression sets the coordinate axis at the centre of the image area. The parameter A_1^{Im} is the desired magnitude of A_1 in the image area and δ is a measure of the width of the transition region between the image and non-image areas. The parameter δ thus represents the steepness of the wettability gradients on a chemically patterned substrate. This method is simple to implement but has certain drawbacks. A large value of δ is necessary in order for the wettability gradients to be gradual and lubrication theory to be valid (see § 2.2), but for a smaller image size this may prevent the function from ever reaching the desired maximum, A_1^{Im}. An example is given in figure 3, in which $A_1(x)$ given by (2.23) for $x < 0$, with $I = 0.3$ and $\delta = 0.01$, is represented by a dashed line. Note that the function never reaches the desired value $A_1^{Im} = 1$. Gradual slopes can also lead to finite $A_1(x)$ slopes at the edges of the simulation domains, which are a problem since they make for a slope discontinuity in applying periodic boundary conditions. Despite its drawbacks, however, the expression is convenient to use and was employed in several of our simulations.

For simulations in which a greater degree of control over $A_1(x)$ was desired, a new piecewise function was employed. This function exactly reaches the desired limits ($A_1(x) = 0$ on non-image areas and $A_1(x) = A_1^{Im}$ on the image areas) with gradual slopes and continuous first and second derivatives throughout. The functions used to connect the flat regions could be considered as flat circles, as they follow an equation similar to that of a circle ($r^4 = x^4 + y^4$) but have flatter edges. These functions have regions with second derivatives equal to zero, which is their chief benefit. Pieces of

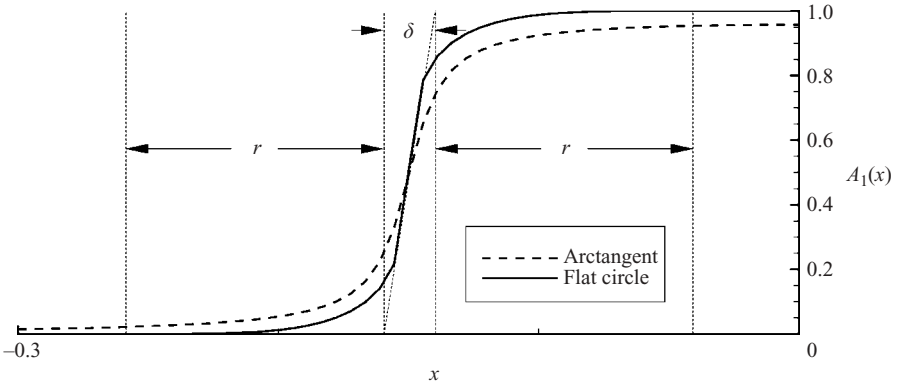

FIGURE 3. Comparison of two different functions used to represent $A_1(x)$ in the simulations. The dashed line represents the arctangent method, (2.23), and the solid line represents the flat-circle method, (2.24). The two lines cross at $x = -I/2$.

a pair of stretched and shifted flat circles can be used to transition smoothly from regions where $A_1 = 0$ to regions where $A_1 = A_1^{Im}$, with a desired slope. The equations for each piece are

$$A_1(x) = \begin{cases} 0, & x \leqslant x_1 \\ \dfrac{A_1^{Im}}{2r}\left\{ r - \left| r^4 - \left(x - \dfrac{A_1(x)\delta}{A_1^{Im}} - x_1\right)^4 \right|^{1/4} \right\}, & x_1 < x \leqslant -I/2 \\ \dfrac{A_1^{Im}}{2r}\left\{ r + \left| r^4 - \left(x - \dfrac{A_1(x)\delta}{A_1^{Im}} - x_2 + \delta\right)^4 \right|^{1/4} \right\}, & -I/2 < x \leqslant x_2 \\ A_1^{Im}, & x_2 < x, \end{cases} \tag{2.24}$$

where $x_1 = (-1/2)(I + \delta) - r$ and $x_2 = (-1/2)(I - \delta) + r$. For the curving sections, $A_1(x)$ is obtained by solving the nonlinear equation with Newton's method. With this flat-circle technique, the curvature (via parameter r) and slope (with parameter δ) of $A_1(x)$ can be controlled independently. The piecewise function is plotted, for $I = 0.3$, $\delta = 0.01$, $r = 0.1$, and $A_1^{Im} = 1$, with a solid line in figure 3, and labelled to indicate how the parameters δ and r contribute to the function's shape.

The periodic boundary conditions specify that the length of the simulation domain is equal to the period length, P, indicated in figure 1. A set of simulations was performed to contrast the effects of including multiple image regions within the periodic domain as against including only the single region described above. These simulations revealed that rupture times and interfacial profiles did not change when multiple image areas were included, verifying that the periodic boundary conditions are sufficient to account for any short- or long-range cooperative processes that might occur between the separate image regions.

3. Interfacial behaviour between homogeneous surfaces

Before examining the behaviour of the liquid–liquid interface between heterogeneous surfaces, it is valuable to understand its behaviour between homogeneous surfaces. We first consider the linear stability of (2.20), then perform simulations to examine the nonlinear behaviour that develops over time.

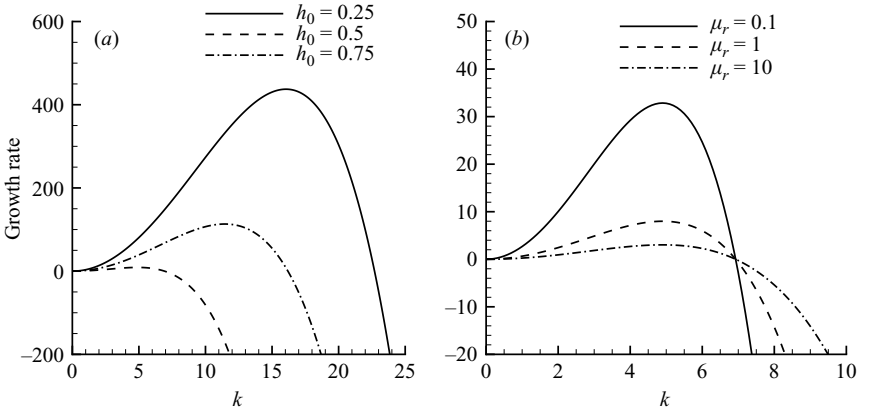

FIGURE 4. Plots of growth rate α versus wavenumber k for different initial heights h_0 and viscosity ratios μ_r. Here $A_1 = 2$, $A_2 = 1$, and $\gamma = 1$. (*a*) Variation in h_0 with $\mu_r = 1$, and (*b*) variation in μ_r with $h_0 = 0.5$.

3.1. *Linear stability analysis*

Application of standard linear stability analysis to (2.20) yields an expression for the dimensionless growth rate, α:

$$\alpha = \frac{k^2[h_0(\mu_r - 1) + 1]}{f(h_0, \mu_r)} \left[A_1 \frac{(1 - h_0)^3}{h_0} + A_2 \frac{h_0^3}{1 - h_0} - k^2 \gamma h_0^3 (1 - h_0)^3 \right], \tag{3.1}$$

where k is a dimensionless real-valued wavenumber and h_0 is the dimensionless initial interfacial height, $h_0 = h_1 / h_{tot}$. This expression is consistent with those obtained by Joo & Hsieh (2000) and Merkt *et al.* (2005). The growth rate is purely real, with positive (negative) values indicating instability growth (decay). Figure 4 shows α versus k for various initial heights and viscosity ratios. An asymmetric attraction of the interface to the lower surface is considered, with $A_1 = 2$, $A_2 = 1$, and $\gamma = 1$. The interface is stabilized for short waves ($k > k_c$) but is destabilized by long waves ($k < k_c$), the maximum growth rate occurring at k_{md}. Expressions for k_c and k_{md} can be obtained analytically from (3.1), with cutoff wavenumber

$$k_c = \left[\frac{1}{\gamma} \left(\frac{A_1}{h_0^4} + \frac{A_2}{(1 - h_0)^4} \right) \right]^{1/2}, \tag{3.2}$$

and the most dangerous wavenumber as $k_{md} = k_c / 2^{1/2}$. For the cases shown in figure 4(*a*) the interface is most unstable for a smaller initial height, such as $h_0 = 0.25$, owing to the close proximity to the highly attractive lower surface, and most stable far from both attractive surfaces, as when $h_0 = 0.5$. The non-monotonic behaviour of k_{md} as h_0 is varied reflects the changing importance of surface-tension forces relative to van der Waals forces in (3.2). The former are larger than the latter near $h_0 = 0.5$, which leads to damping of short-wavelength disturbances and relatively small values of k_{md}. Figure 4(*b*) shows that variations in μ_r have no effect on k_c and k_{md} but a significant effect on the growth rate. Interfacial disturbances will grow much more slowly at high μ_r, owing to viscous dissipation.

Figure 5 shows initial and rupture interfacial profiles from a simulation of (2.20) with $A_1 = 1$, $A_2 = 0$, $\gamma = 1$, $\mu_r = 1$, and $h_0 = 0.5$ and domain size $3\lambda_{md}$. Here λ_{md} is the most dangerous wavelength and is given by $2\pi / k_{md}$. The simulation starts with a randomly perturbed interface, generated in the manner described in § 2.3 for

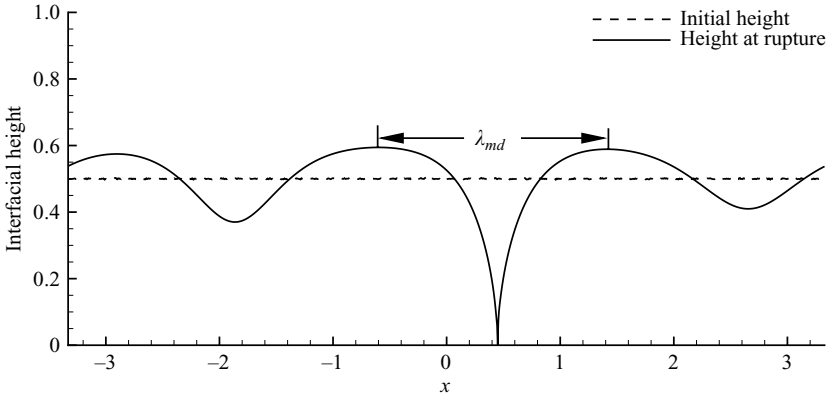

FIGURE 5. Interfacial profiles initially and at rupture for a homogeneous van der Waals attraction. This simulation has a domain length of $3\lambda_{md}$, with $A_1 = 1$, $A_2 = 0$, $\gamma = 1$, $\mu_r = 1$, and $h_0 = 0.5$. Rupture occurs at a dimensionless time $t_r = 7.3$ and is driven by the wettability of the lower surface.

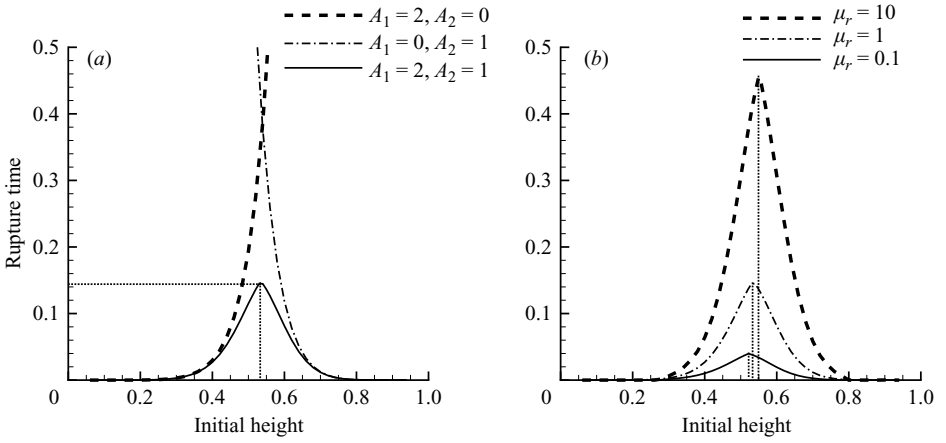

FIGURE 6. Variation in rupture time t_r with initial height h_0 for (a) various sets of Hamaker constants and (b) various viscosity ratios μ_r. In (a) $\mu_r = 1$ and in (b) $A_1 = 2$ and $A_2 = 1$; $\gamma = 1$ in both plots. When both Hamaker constants are non-zero, the rupture times reach a maximum, when rupture occurs simultaneously on both bounding surfaces. The corresponding initial height is denoted $h_0 = h_0^*$ and is indicated by a vertical dashed line in the above plots.

the heterogeneous case, and ends with rupture and verification that the most rapidly growing disturbance has wavelength λ_{md}. These results provide a justification for using the simple initial conditions for the homogeneous case that were described in § 2.3 and will serve as an important contrast to the rupture profiles between heterogeneous surfaces presented in § 4.

3.2. *Film rupture between homogeneous surfaces*

We focus on the behaviour of the rupture time, t_r, in our study for two reasons. First, as will be seen in § 4, variations in the rupture time indicate variations in the rupture mechanism. Second, the rupture time is a key time scale for applications where either the maintenance of a uniform liquid film or the creation of patterns via intentional ruptures is desired. Figure 6 shows typical plots of rupture time versus initial height. In figure 6(a), each curve corresponds to a different set of Hamaker constants, with

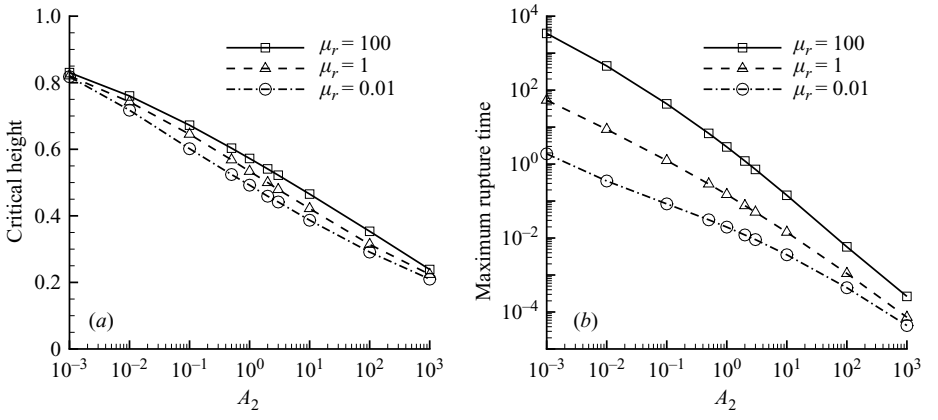

FIGURE 7. Plots of (*a*) critical height h_0^* and (*b*) maximum rupture time t_r^{max} vs. A_2 for viscosity ratio $\mu_r = 0.01$, 1, and 100. In each simulation, $A_1 = 2$ and $\gamma = 1$.

$\gamma = 1$ and $\mu_r = 1$. The presence of an attraction only to the lower solid ($A_1 = 2$, $A_2 = 0$) leads to a very small rupture time for small h_0 values, since the interface is in close proximity to the attractive solid. The increase in rupture time with larger h_0 values is very rapid, since the magnitude of the van der Waals force decreases as h^{-3}. Even for very large values of h_0, rupture always occurs in a finite amount of time. The curves for $A_1 = 0$ and $A_2 = 1$ in figure 6(*a*) show analogous behaviour. Since the attraction is smaller than in the previous case, the rupture times increase more rapidly. The shapes of these two curves together are suggestive of what the curve looks like for an interface attracted to both solid boundaries at the same time, a case considered by Joo & Hsieh (2000) only for symmetric Hamaker constants. The third curve of figure 6(*a*) shows that when $A_1 = 2$ and $A_1 = 1$ the rupture times approach zero as $h_0 \to 0$ or $h_0 \to 1$, when the interface is near each attractive surface. The rupture times increase more gradually with distance from the attractive solids than in the previous cases since the interface is subject to cooperative attractions in both directions. The most significant point is the maximum rupture time, t_r^{max}, which occurs at nearly the same initial height as the height where the previous curves cross. This initial height, labeled h_0^*, marks the initial condition that will lead to a simultaneous rupture on both bounding surfaces. Interfacial rupture will occur first on the lower surface for smaller initial heights, or the upper surface for larger initial heights. Here $h_0^* > 0.5$, since the stronger attraction to the lower surface will cause interfacial rupture to occur there first for a wider range of initial heights.

The values of h_0^* and t_r^{max} can be determined for any set of A_1, A_2, γ, and μ_r. Figure 6(*b*) ($A_1 = 2$, $A_2 = 1$, and $\gamma = 1$) shows that increasing the viscosity ratio leads to an expected increase in t_r^{max} but also a slight increase in h_0^*. Thus, as the top layer becomes more viscous, rupture occurs there first for a smaller range of initial heights. Figure 7 shows the dependence of t_r^{max} and h_0^* on the Hamaker constants and the viscosity ratio in more detail, with $A_1 = 2$ and $\gamma = 1$. As A_2 increases, both h_0^* and t_r^{max} decrease, which is indicative of the increased range of the interfacial attraction to the upper surface. Increases in μ_r lead to increases in h_0^* and t_r^{max}, consistently with figure 6(*b*).

Figure 8 shows the rupture-time curves for different values of the interfacial tension and makes clear the dependence of h_0^* and t_r^{max} on this parameter. An increase in γ by any factor will shift the entire t_r curve upward by this same factor, thereby

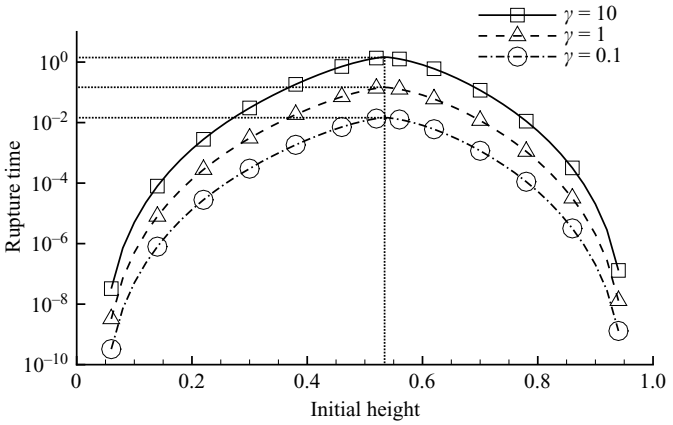

FIGURE 8. Rupture time (t_r) variation with initial height (h_0) for different interfacial tensions (γ) with $A_1 = 2$, $A_2 = 1$, and $\mu_r = 1$. The logarithmic scaling shows that as γ increases by a factor of 10, so does t_r. The value of h_0^* does not vary with interfacial tension.

keeping h_0^* constant. The interfacial tension acts as a retarding force for rupture, so the increase in rupture time is certainly expected. The exactness of the effect can be explained by examining the two important limits of the evolution, the initial and final growth. The growth rate of the initial disturbance is given by (3.1), and substitution of the expression for k_{md} into this equation shows that the initial growth rate is inversely proportional to γ. By 'final growth' we refer to the approach of the interface to the singularity of film rupture. Zhang & Lister (1999) constructed similarity solutions for this approach in the case of a single liquid film, finding that the minimum interfacial height decreased with $(t_r - t)^{1/5}$, where $t_r - t$ is the time until rupture and is proportional to the surface tension. This single-liquid result can be extended to the case of stratified liquid films via a simple scaling analysis and shows that the time until rupture will indeed be proportional to γ. Thus both the initial and final limits of evolution exhibit the same dependence on the interfacial tension, leading to the expected effect on the rupture time.

4. Interfacial behaviour between heterogeneous surfaces

We first discuss the roles of wettability gradients, image size, and period size on rupture-time behaviour and then examine the underlying mechanisms. The results of a parametric study are also presented.

4.1. *Roles of wettability gradients and image size*

Two important horizontal length scales arise in the simulations with heterogeneous surfaces. The first is the 'natural' length scale, given by the value of λ_{md} for a homogeneous surface ($I = P$). The second is the 'imposed' length scale, given by the image size I. The presence of this second length scale leads to very different rupture behaviour, as shown in figure 9. Here $A_1(x)$ is given by (2.23), with $\delta = 0.01$, $A_1^{Im} = 1$, and $I = 0.65P$. Rupture appears to occur at two locations, both near the edges of the image area. Asymmetry in the initial condition causes rupture to occur at the left-hand edge first; symmetric initial conditions lead to simultaneous rupture with insignificant rupture-time variation. Figure 9 can be contrasted with figure 5, which corresponds to a homogeneous surface ($I = P$) and has all other parameters the

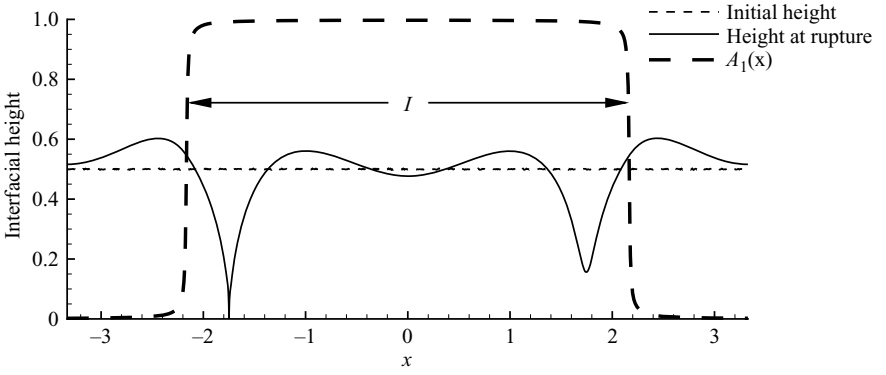

FIGURE 9. Interfacial profiles initially and at rupture for a spatially-varying van der Waals attraction. Here $A_1(x)$ is generated by the arctangent method with $\delta = 0.01$, $A_1^{Im} = 1$, and $I = 0.65P$. This simulation has a domain length of $3\lambda_{md}$, with $A_1 = 1$, $A_2 = 0$, $\gamma = 1$, $\mu_r = 1$, and $h_0 = 0.5$. Rupture occurs at a dimensionless time of $t_r = 0.9$.

same. The key difference between the two is the action of wettability gradients in the heterogeneous case, described in § 2.1 and below. These gradients lead to rupture times approximately an order of magnitude faster than the corresponding homogeneous case ($t_r = 0.9$ versus $t_r = 7.3$ for the homogeneous case).

Also captured in figure 9 is evidence of an emulsification mechanism. This mechanism is initiated by the two nearly simultaneous ruptures of the film of liquid 1, which allow liquid 2 to contact the lower surface. Since liquid 2 preferentially wets the image area, spreading of liquid 2 from each rupture location would occur, with pockets of liquid 1 becoming trapped when multiple spreading fronts of liquid 2 contact each other. Such emulsification is a recognized characteristic of the lithographic printing process, in that some water is always entrained in the ink that is transferred to the printing plate.

Variation in the image sizes will lead to very distinct variations in rupture time, as first noted by Konnur *et al.* (2000) in their study of single liquid films dewetting on chemically heterogeneous substrates. For the case of an isolated image area, they reported that rupture times are only independent of image size when that size is above a certain critical value. A plot of rupture time versus image size is given in Kargupta *et al.* (2000). An analogous plot for the case of stratified films is given in figure 10, which also shows curves for various domain (period) sizes. This plot differs from that given in Kargupta *et al.* (2000) by encompassing both small image and small non-image areas (non-isolated patterns). In considering only small images, the plot in this paper terminates in a plateau on the right-hand side.

The rupture-time curves for four different period sizes given in figure 10 share some generic features. The peaks and valleys on the left-hand side of each curve result from effects due to small image areas, and the features on the right-hand side of each curve correspond to small non-image areas. Each curve shows the limit of no attraction ($t_r \to \infty$ as $I \to 0$) and homogeneous attraction (as $I \to P$). For larger domains ($P = 3\lambda_{md}$ and $5\lambda_{md}$) the left- and right-hand side features are connected by a plateau region. The smallest integer multiple of λ_{md} to exhibit all the above features is $P = 3\lambda_{md}$, which was chosen for our study. In the following section, we probe the mechanisms underlying the various generic features of the rupture-time behaviour.

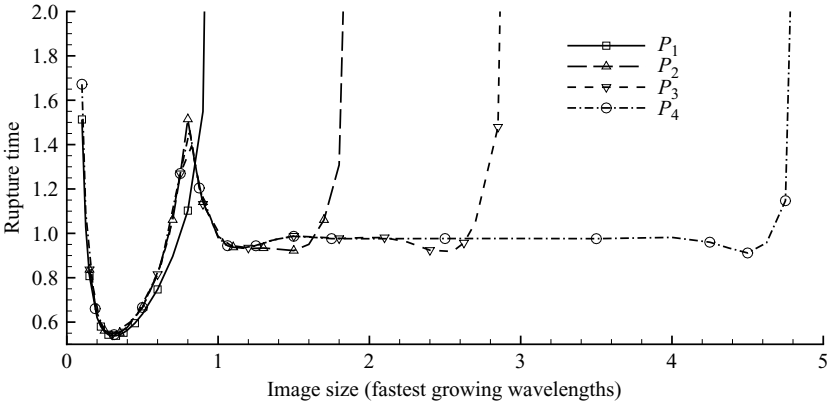

FIGURE 10. Variation in the rupture time as a function of image size for period sizes $P_1 = \lambda_{md}$, $P_2 = 2\lambda_{md}$, $P_3 = 3\lambda_{md}$, and $P_5 = 5\lambda_{md}$. Each curve reaches the zero-image limit ($t_r \to \infty$) at the far left of the plot but reaches the full-image limit at different points along the x- axis. The images were generated by the arctangent method, with $\delta = 0.01$ and $A_1^{Im} = 1$. In all cases $h_0 = 0.5$ and $\mu_r = \gamma = 1$.

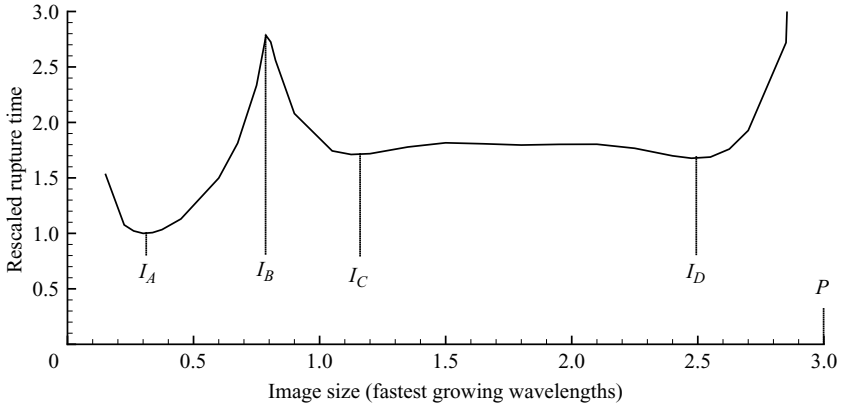

FIGURE 11. Variation in rescaled rupture time with image size. Here, we replot the data given for $P = 3\lambda_{md}$ in figure 10 but scale the rupture time by the value which occurs at the global minimum. Image sizes at which important curve features occur are also marked.

4.2. *Mechanisms underlying rupture-time behaviour*

The results for $P = 3\lambda_{md}$ shown in figure 10 can be rescaled by replacing t_r with t_r/t_r^{min} on the ordinate, where t_r^{min} is the global minimum of the rupture time. The minimum rupture time now occurs at $t_r/t_r^{min} = 1$, as shown in figure 11. As will be seen in § 4.3, the behaviour of this rescaled rupture time is relatively robust to changes in the various problem parameters. The image sizes at which four important curve features occur have been labeled I_A, I_B, I_C, and I_D. Each feature corresponds to a distinct interfacial profile resulting from a particular pathway to film rupture. To illustrate this, figure 12 shows the shape of the liquid interface at rupture for the four critical image sizes, along with the function $A_1(x)$ to indicate the boundaries of the image (the flat-circle method, $r = 0.1$, $\delta = 0.01$). The mechanisms that lead to the features at image sizes I_A and I_B for a single liquid film were discussed qualitatively by Kargupta *et al.* (2000). We will proceed with a more quantitative analysis of the stratified case

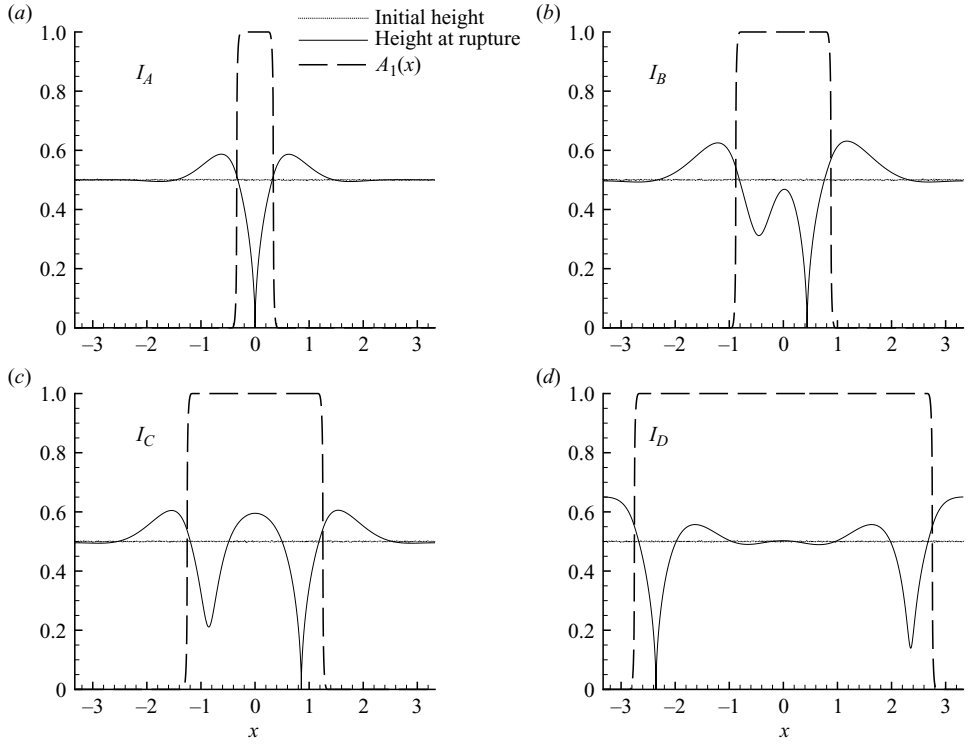

FIGURE 12. Interfacial profiles at rupture for the four critical image sizes indicated in figure 11.

by examining the three flow-rate components involved in the rupture process; cf. (2.22).

The profile shown in figure 12(*a*) represents the global minimum of the rupture time and corresponds to image size I_A. Figure 13 shows plots of the three flow-rate components of liquid 1 for three different stages of evolution: 20 % completion, 90 % completion, and over 99 % completion. The bold line in each plot is the overall flow rate, and the location of eventual rupture is indicated by the behaviour of this curve. We may call this location x_r; here the overall flow rate of liquid 1 is zero but the slope of the flow-rate curve is positive, so for this image size $x_r = 0$. The liquid in film 1 left of x_r is driven to the left (negative flow rate), and the liquid to the right of x_r is driven to the right (positive flow rate). As liquid 1 is driven away from this point it is replaced by liquid 2, a process which continues until liquid 2 makes contact with solid 3 at rupture. Regardless of image size, in the early stages of evolution the dominant flow is due to wettability gradients (and the oppositional capillary flow). These gradients act to locally thin liquid 1 near the edges of the image, which are located at the flow-rate spikes in figure 13(*a*). Figure 13(*b*) shows that as the film is thinned further the wettability contribution begins to become important. At x_r the wettability flow rate is also zero, sloping positively, but is opposed by the negatively sloping capillary-flow rate. Finally, near the time of rupture, the wettability component begins to dominate (figure 13*c*). The increase in relative magnitude of the wettability driven flow can be attributed to its being proportional to $1/h^4$, while the wettability-gradient flow rates are only proportional to $1/h^3$. Thus, the film of liquid 1 thins relatively slowly initially, but much more rapidly as rupture is approached.

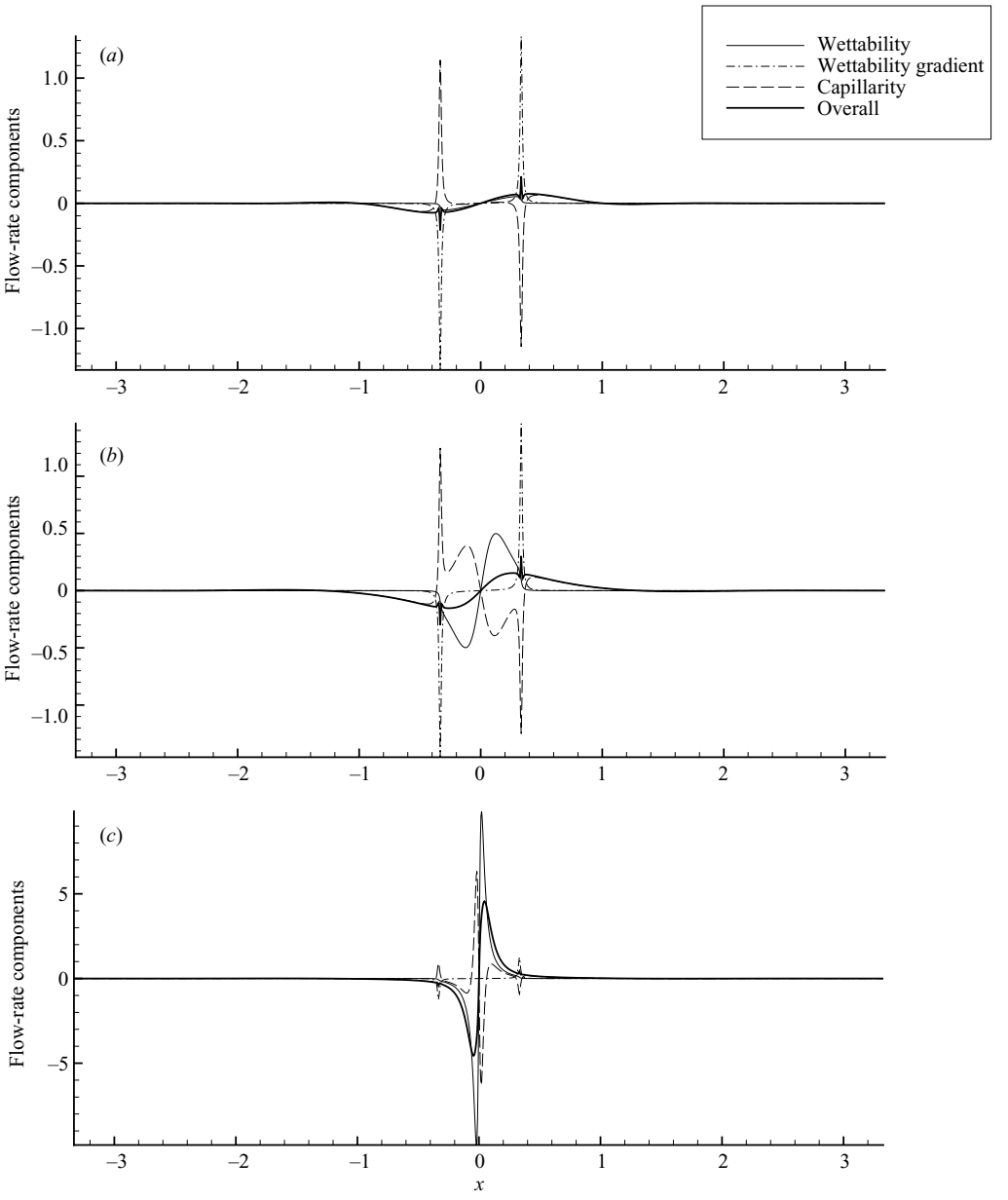

FIGURE 13. The three flow-rate components of liquid 1 and their sum for interfacial evolution above an image of size I_A at (*a*) 20 % completion, (*b*) 90 % completion, and (*c*) over 99 % completion.

The image size I_A corresponds to a global minimum of the rupture time because of the cooperation of the wettability and wettability-gradient flow rates. The image is small enough that the wettability gradients on both edges of the image may cooperate to thin liquid 1 at the image centre. Each gradient acts to drive liquid 1 away from the image area, and wettability effects add to this gradient-driven flow as the film becomes even thinner. Thus, I_A could be thought of as the optimum length scale for film rupture, which for the base case is equal to $0.3\lambda_{md}$. Throughout the remainder

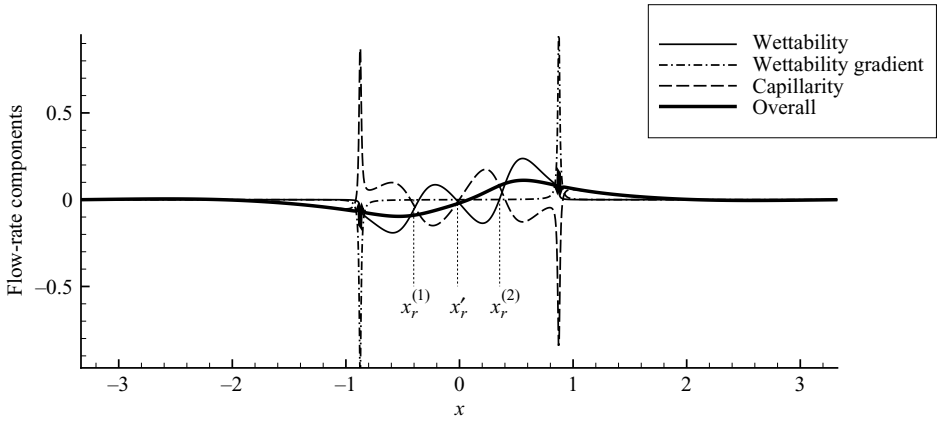

FIGURE 14. The three flow-rate components of liquid 1 and their sum for interfacial evolution above an image of size I_B at 90 % completion.

of the paper this will be referred to as the 'rupture' length scale, the image size corresponding to the most rapid rupture of the lower film.

An increase in image size begins to put the driving forces for rupture into conflict, leading to the rupture profile shown in figure 12(*b*). Here the image size I_B is large enough for two separate regions of the lower film to be thinned by wettability gradients, each region occurring just inside the edges of the image. This is again seen in the flow-rate plot for 90 % completion in figure 14. At the point x_r' at the image centre, the overall flow rate equals zero and has a positive slope indicating that liquid 1 is being driven away on either side. However, the wettability flow rate equals zero with a negative slope at this point, indicating that the wettability term is actually driving flow towards x_r'. Since it has been shown that the wettability term is dominant near rupture, this suggests that rupture will not occur at this location. Instead, rupture appears more likely to occur at the two neighbouring points at which the wettability flow rate is zero with a positive slope, $x_r^{(1)}$ and $x_r^{(2)}$. The proximity of these points to each other is a major reason for the increase in rupture time. The length of the image area, I_B, is $0.8\lambda_{md}$, which suggests that if two ruptures with the optimum rupture length of $0.3\lambda_{md}$ form then they would be separated by only the small distance of $0.2\lambda_{md}$. (We note that two ruptures can form simultaneously at this image size if a symmetric initial condition is used.) As will be seen below, $0.2\lambda_{md}$ is less than the optimum separation length scale, leading to regions of high curvature and strong opposition from capillary flows. This opposition is eventually overcome by wettability-driven flows but not before an increase in rupture time occurs.

Cooperation between driving forces is again possible with a further increase in the length of the image. Figure 12(*c*) shows the interfacial profile at rupture for image size I_C, and the flow-rate plot for 90 % completion in figure 15 suggests why the rupture time is considerably smaller than in the previous case. Here, a pair of points, $x_r^{(1)}$ and $x_r^{(2)}$, follows the rupture behaviour described with respect to image size I_A: the overall flow rate equals zero with a positive slope, being driven by the positive-sloping wettability flow rate (which drives liquid 1 away from each $x_r^{(i)}$). In contrast with the flow rates shown for image size I_B (figure 14), the capillary flow rate is negligible at the centre of the image. In this case, the thinned regions are far enough apart that the interface can hold the displaced liquid 1 at the image centre below a region of reduced curvature. Therefore nearly simultaneous ruptures may form more easily at $x_r^{(1)}$ and

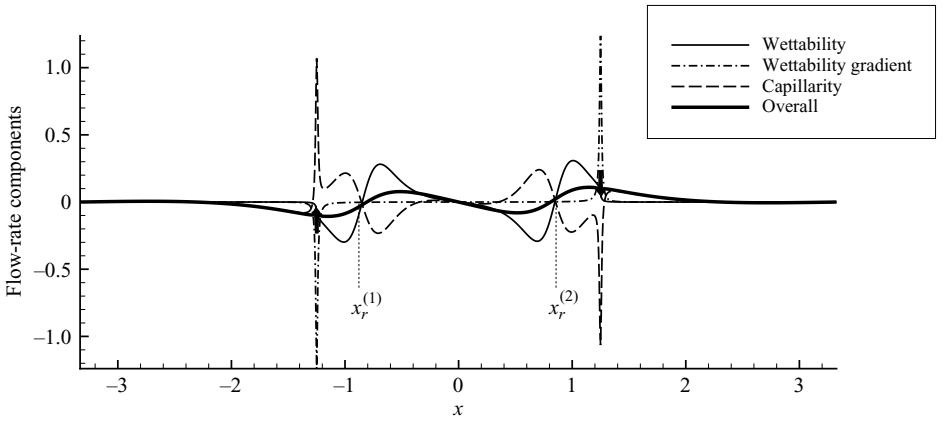

FIGURE 15. The three flow rate components of liquid 1 and their sum for interfacial evolution above an image of size I_C at 90 % completion.

$x_r^{(2)}$. Note that since $I_C = 1.1\lambda_{md}$ and the length scale of each of the two ruptures is again the optimum length scale, $0.3\lambda_{md}$, the centre region has length $0.5\lambda_{md}$. This 'separation' length scale is larger than the $0.2\lambda_{md}$ distance between ruptures for image size I_B and will be referred to again shortly.

An increase in the image size to a length between the lengths of I_C and I_D results in a rupture time in the plateau region of figure 11. An interfacial profile in this region was shown in figure 9, in which ruptures appear to occur near the two image edges with only a slightly curved interface above the image centre. The flow-rate plot is qualitatively similar to that shown in figure 15. In the plateau region, the ruptures at the image edges are essentially independent of each other, which is consistent with zero flow rate at the image centre.

The next important limit occurs when the distance between image areas is small enough for interaction across non-image areas. The corresponding interfacial profile is shown in figure 12(*d*), where $I = I_D$. The flow-rate plot is again qualitatively similar to that corresponding to the image size I_C (figure 15). Now, however, the smallest region between the rupture points is a non-image area, which lacks a van der Waals attraction. Without this attraction to retard the interface as it is driven upwards by the displaced liquid 1 (which is being driven off the image areas onto the non-image areas), rupture will occur slightly faster. The significant length scale here is not I_D but $P - I_D$, the length of the non-image area. This is the same separation length scale mentioned in conjunction with image size I_C and is approximately equal to $0.5\lambda_{md}$. As with I_C, a minimum in the rupture time is observed for this image size.

4.3. *Parametric study*

We now explore how the rescaled rupture-time curve, figure 11, changes as various problem parameters are varied. As an example, figure 16 shows several curves corresponding to different viscosity ratios μ_r. The basic effect of an increase in μ_r is an increase in the rupture time, as discussed in § 3.2. In terms of the rescaled rupture-time curve, we see that the effect of a viscous top layer on the curve shape is minor. One apparent trend is the increase in the lengths of I_A, I_B, and I_C with μ_r. Also the 'span' of the plot, or difference between the rescaled rupture times corresponding to the global minimum and the nearby steep maximum, increases with μ_r. In contrast, the separation length scale $P - I_D$ does not change with the viscosity ratio. In fact,

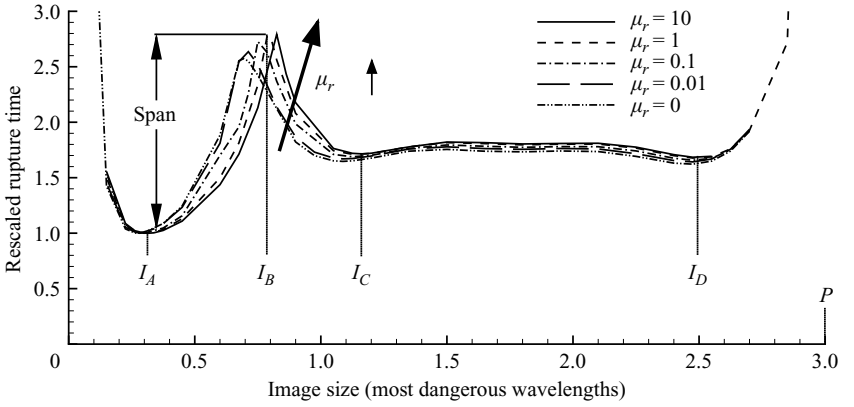

FIGURE 16. Variation in the rescaled rupture-time plot with viscosity ratio μ_r with $A_1(x)$ given by the arctangent method. $A_1^{Im} = 1$, $\delta = 0.01$, $h_0 = 0.5$, and $\gamma = 1$.

Parameter being increased	Effect on t_r	Effect on $I_{A,B,C}$	Effect on span
μ_r	increase	increase	increase
h_0	increase	increase	increase
δ	increase	increase	decrease
γ	increase	no change	increase
A_1^{Im}	decrease	increase	decrease

TABLE 1. Effects of parameter variation on the rescaled rupture-time plot.

this length scale will not change with any variation in the problem parameters, thus affirming its significance. Another surprising constant is the interaction between certain length scales. For any variation in the problem parameters, the value of I_C can be determined as a function of the separation and rupture length scales:

$$I_C = 2I_A + P - I_D. \tag{4.1}$$

This relationship can be conjectured by recognizing that the shape of the interface at rupture for image size I_C (figure 12*c*) appears to consist of two ruptures having the optimum rupture length scale I_A and separated by the optimum separation length scale $P - I_D$. This equality was valid for every simulation we conducted. The value for I_B does not have such an exact relationship but clearly does depend on the same length scales. An approximate empirical relationship is

$$I_B \approx I_A + 0.6(I_C - I_A). \tag{4.2}$$

The effect of varying other parameters on the key features of the rescaled rupture-time curve is summarized in table 1. Only the simulations in which μ_r was varied used the arctangent function to describe the spatial variation in $A_1(x)$; the method of 'flat-circles' was used in the other cases because of the need for precise slope control. The effects on rupture time shown here are simple to understand and again follow the patterns set forth in § 3.2. Not covered in that discussion, however, was the effect of physical wettability gradients on rupture time. An increase in the parameter δ decreases the magnitude of the wettability gradients and the flows driven by them, thereby leading to an increase in rupture time. We note that for values of δ less

than 0.01, the rupture time decreases by less than 0.2 %. However, increasing δ to 0.5 results in a 10 %–15 % increase in rupture time.

Clear trends are also observed for the length scales I_A, I_B, and I_C, which increase with an increase in any problem parameter except for γ, and the span for each curve. Since $P - I_D$ is constant with any parameter variation and the length scales I_B and I_C are strongly dependent on the rupture length scale I_A, the length-scale increases can be examined solely as an increase in I_A. Changes in the span indicate differences in the relative speed of rupture for image sizes I_A and I_B, beyond that which was accounted for by a rescaling of the rupture time. Although each parameter change given in table 1 leads to a very particular trend in the curve shape, a single simple theory justifying each trend appears unlikely. Nevertheless, figure 16 and table 1 illustrate that the shape of the rescaled rupture-time curve is remarkably robust to changes in the problem parameters.

5. Conclusions

We have studied the behaviour of stratified thin liquid films between parallel surfaces under conditions where van der Waals forces drive dewetting. Lubrication theory was applied to derive a nonlinear evolution equation for the interfacial height, and its linear stability and nonlinear behaviour were investigated. In the case where the bounding solid surfaces are chemically homogeneous, the two films can undergo a competitive displacement in which one film tries to displace the other from the surface with which it was originally in contact. At a critical value of the initial interfacial height, rupture occurs simultaneously on both bounding surfaces and the rupture time exhibits a maximum.

Chemical heterogeneity introduces an additional competition between the length scale of the heterogeneity and the most dangerous wavelength for the corresponding homogeneous surface. This competition leads to a strong dependence of the rupture time on the ratio of these length scales. Film thinning and displacement are initiated by wettability gradients at the edges of the image areas (which represent the heterogeneity) and are accelerated by the wettability itself, close to film rupture. If the image area is narrow enough then only a single rupture will occur, whereas if it is above a certain width then a rupture will occur near each of the image-area edges. When these two ruptures do occur they will interact strongly with each other via capillary forces if the image area is still rather narrow and produce a maximum in the rupture time. Widening the image area causes the two ruptures to occur independently, and when the non-image area becomes sufficiently narrow, the ruptures again interact but across the non-image areas. The maximum and minima observed in the rupture time (figure 11) can be understood in terms of optimum length scales for rupture and for the separation distance between ruptures. The behaviour of the rescaled rupture time is also found to be relatively independent of changes in the other problem parameters.

The present work bridges an important gap between previous work on stratified thin liquid films between chemically homogeneous surfaces and work on single thin liquid films on chemically heterogeneous substrates. In particular, the configuration considered here is especially relevant to the lithographic printing process. Results from our nonlinear simulations in the heterogeneous case suggest a mechanism by which one liquid can be emulsified into the other. As the degree of emulsification will affect print quality, our results imply that it should be possible to control this through the size of the image area (or the size of the pixels that comprise an image area). Although

a number of other factors are likely to be important (e.g. shear, substrate porosity and roughness, non-Newtonian rheology), the present work provides a starting point for accounting for those effects.

Another issue worthy of pursuit is the effect of a short-range repulsion on the results described above. Although it would not change the initial thinning of the lower layer due to wettability gradients, it would eliminate the singularity which occurs at film rupture and allow the system to continue to evolve to a steady configuration. Such steady patterns could play a role in microfluidic devices for creating droplet arrays, which are of considerable interest for applications requiring reproducible parcels of liquids in multiphase flows (Squires & Quake 2005).

This work was supported through the Industrial Partnership for Research in Interfacial and Materials Engineering of the University of Minnesota. We are especially grateful for a gift from the Dai Nippon Printing Company. We also thank 3M for their support of a graduate fellowship to R. D. L.

REFERENCES

Benney, D. J. 1966 Long waves on liquid films. *J. Math. Phys.* **45**, 150–155.

Bischof, J., Scherer, D., Herminghaus, S. & Leiderer, P. 1996 Dewetting modes of thin metallic films: Nucleation of holes and spinodal dewetting. *Phys. Rev. Lett.* **77**, 1536–1539.

Burelbach, J. P., Bankoff, S. G. & Davis, S. H. 1988 Nonlinear stability of evaporating/condensing liquid films. *J. Fluid Mech.* **195**, 463–494.

Danov, K. D., Paunov, V. N., Alleborn, N., Raszillier, H. & Durst, F. 1998*a* Stability of evaporating two-layered liquid film in the presence of surfactant–I. The equations of lubrication approximation. *Chem. Engng Sci.* **53**, 2809–2822.

Danov, K. D., Paunov, V. N., Stoyanov, S. D., Alleborn, N., Raszillier, H. & Durst, F. 1998*b* Stability of evaporating two-layered liquid film in the presence of surfactant–II. Linear analysis. *Chem. Engng Sci.* **53**, 2823–2837.

Decré, M. M. J. & Baret, J.-C. 2003 Gravity-driven flows of viscous liquids over two-dimensional topographies. *J. Fluid Mech.* **487**, 147–166.

Fisher, L. S. & Golovin, A. A. 2005 Nonlinear stability analysis of a two-layer thin liquid film: Dewetting and autophobic behaviour. *J. Colloid Interface Sci.* **291**, 515–528.

Hamaker, H. C. 1937 The London–van der Waals attraction between spherical particles. *Physica* **4**, 1058–1072.

Harrey, P. M., Evans, P. S. A., Ramsey, B. J. & Harrison, D. 1999 A novel manufacturing process for capacitors using offset lithography. In *First Intl Symp. on Environmentally Conscious Design and Inverse Manufacturing*, pp. 842–846. Tokyo, Japan.

Jensen, O. E. & Grotberg, J. B. 1992 Insoluble surfactant spreading on a thin viscous film: shock evolution and film rupture. *J. Fluid Mech.* **240**, 259–288.

Jensen, O. E. & Grotberg, J. B. 1993 The spreading of heat or soluble surfactant along a thin liquid film. *Phys. Fluids* A **5**, 58–68.

Joo, S. W. & Hsieh, K.-C. 2000 Interfacial instabilities in thin stratified viscous fluids under microgravity. *Fluid Dyn. Res.* **26**, 203–217.

Kalliadasis, S., Bielarz, C. & Homsy, G. M. 2000 Steady free-surface thin film flows over topography. *Phys. Fluids* **12**, 1889–1898.

Karapanagiotis, I. & Gerberich, W. W. 2005 Polymer film rupturing in comparison with leveling and dewetting. *Surf. Sci.* **594**, 192–202.

Kargupta, K., Konnur, R. & Sharma, A. 2000 Instability and pattern formation in thin liquid films on chemically heterogeneous substrates. *Langmuir* **16**, 10243–10253.

Kargupta, K. & Sharma, A. 2002 Morphological self-organization by dewetting in thin films on chemically patterned substrates. *J. Chem. Phys.* **116**, 3042–3051.

Kheshgi, H. S. & Scriven, L. E. 1991 Dewetting: Nucleation and growth of dry regions. *Chem. Engng Sci.* **46**, 519–526.

Konnur, R., Kargupta, K. & Sharma, A. 2000 Instability and morphology of thin liquid films on chemically heterogeneous substrates. *Phys. Rev. Lett.* **84**, 931–934.

Kumar, S. & Matar, O. K. 2004 Dewetting of thin liquid films near soft elastomeric layers. *J. Colloid Interface Sci.* **273**, 581–588.

Leyland, N. S., Evans, J. R. G. & Harrison, D. J. 2002 Lithographic printing of force-sensitive resistors. *J. Mater. Sci., Mater. Electron.* **13**, 387–390.

MacPhee, J. 1998 *Fundamentals of Lithographic Printing*. GATFPress.

Matar, O. K. 2002 Nonlinear evolution of thin free viscous films in the presence of soluble surfactant. *Phys. Fluids* **14**, 4216–4234.

Matar, O. K., Gkanis, V. & Kumar, S. 2005 Nonlinear evolution of thin liquid films dewetting near soft elastomeric layers. *J. Colloid Interface Sci.* **286**, 319–332.

Matar, O. K. & Kumar, S. 2004 Rupture of a surfactant-covered thin liquid film on a flexible wall. *SIAM J. Appl. Maths* **64**, 2144–2166.

Mazouchi, A. & Homsy, G. M. 2001 Free surface Stokes flow over topography. *Phys. Fluids* **13**, 2751–2761.

Merkt, D., Pototsky, A., Bestehorn, M. & Thiele, U. 2005 Long-wave theory of bounded two-layer films with a free liquid-liquid interface: Short- and long-time evolution. *Phys. Fluids* **17**, 64104–1–20.

Oron, A., Davis, S. H. & Bankoff, S. G. 1997 Long-scale evolution of thin liquid films. *Rev. Mod. Phys.* **69**, 931–980.

Paunov, V. N., Danov, K. D., Alleborn, N., Raszillier, H. & Durst, F. 1998 Stability of evaporating two-layered liquid film in the presence of surfactant–III. Non-linear stability analysis. *Chem. Engng Sci.* **53**, 2839–2857.

Pototsky, A., Bestehorn, M., Merkt, D. & Thiele, U. 2004 Alternative pathways of dewetting for a thin liquid two-layer film. *Phys. Rev.* E **70**, 25201–1–4.

Pritchard, W. G., Scott, L. R. & Tavener, S. J. 1992 Numerical and asymptotic methods for certain viscous free-surface flows. *Phil. Trans. R. Soc. Lond* A **340**, 1–45.

Ruckenstein, E. & Jain, R. K. 1974 Spontaneous rupture of thin liquid films. *J. Chem. Soc. Faraday Trans.* II **70**, 132–147.

Seemann, R., Herminghaus, S. & Jacobs, K. 2001 Gaining control of pattern formation of dewetting liquid films. *J. Phys.: Condens. Matter* **13**, 4925–4938.

Sharma, A. & Jameel, A. T. 1993 Nonlinear stability, rupture, and morphological phase separation of thin fluid films on apolar and polar substrates. *J. Colloid Interface Sci.* **161**, 190–208.

Sharma, A. & Ruckenstein, E. 1985 Mechanism of tear film rupture and formation of dry spots on cornea. *J. Colloid Interface Sci.* **106**, 12–27.

Sharma, A. & Ruckenstein, E. 1986*a* An analytical nonlinear theory of thin film rupture and its application to wetting films. *J. Colloid Interface Sci.* **113**, 456–479.

Sharma, A. & Ruckenstein, E. 1986*b* The role of lipid abnormalities, aqueous and mucus deficiencies in the tear film breakup, and implications for tear substitutes and contact lens tolerance. *J. Colloid Interface Sci.* **111**, 8–34.

Sheludko, A. 1967 Thin liquid films. *Adv. Colloid Interface Sci.* **1**, 391–464.

Squires, T. M. & Quake, S. R. 2005 Microfluidics: Fluid physics at the nanoliter scale. *Rev. Mod. Phys.* **77**, 977–1026.

Stange, T. G., Evans, D. F. & Hendrickson, W. A. 1997 Nucleation and growth of defects leading to dewetting of thin polymer films. *Langmuir* **13**, 4459–4465.

Stillwagon, L. E. & Larson, R. G. 1988 Fundamentals of topographic substrate leveling. *J. Appl. Phys.* **63**, 5251–5258.

Stillwagon, L. E. & Larson, R. G. 1990 Leveling of thin films over uneven substrates during spin coating. *Phys. Fluids* A **2**, 1937–1944.

Vrij, A. 1966 Possible mechanism for the spontaneous rupture of thin, free liquid films. *Discuss. Faraday Soc.* **42**, 23–33.

Williams, M. B. & Davis, S. H. 1982 Nonlinear theory of film rupture. *J. Colloid Interface Sci.* **90**, 220–228.

de Wit, A., Gallez, D. & Christov, C. I. 1994 Nonlinear evolution equations for thin liquid films with insoluble surfactants. *Phys. Fluids* **6**, 3256–3266.

Witelski, T. P. & Bernoff, A. J. 1999 Stability of self-similar solutions for van der Waals driven thin film rupture. *Phys. Fluids* **11**, 2443–2445.

YIANTSIOS, S. G. & HIGGINS, B. G. 1991 Rupture of thin films: Nonlinear stability analysis. *J. Colloid Interface Sci.* **147**, 341–350.

ZHANG, W. W. & LISTER, J. R. 1999 Similarity solutions for van der Waals rupture of a thin film on a solid substrate. *Phys. Fluids* **11**, 2454–2462.

ZHANG, Y. L., MATAR, O. K. & CRASTER, R. V. 2003 Analysis of tear film rupture: Effect of non-Newtonian rheology. *J. Colloid Interface Sci.* **262**, 130–148.

ZOPE, M., KARGUPTA, K. & SHARMA, A. 2001 Self-organized structures in thin liquid films on chemically heterogeneous substrates: Effect of antagonistic short and long range interactions. *J. Chem. Phys.* **114**, 7211–7221.